Journal of Materials Chemistry

Cite this: J. Mater. Chem., 2011, 21, 7343

www.rsc.org/materials

PAPER

Sonoelectrochemical fabrication of PDDA-RGO-PdPt nanocomposites as electrocatalyst for DAFCs

Jian-Jun Shi,[ab] Guo-Hai Yang[a] and Jun-Jie Zhu*[a]

Received 21st January 2011, Accepted 9th March 2011
DOI: 10.1039/c1jm10333d

Sonoelectrochemical technique was successfully used to fabricate alloy–graphene nanocomposites. It not only provides a simple way to synthesize alloy nanoparticles, but also shows a general strategy for fabricating graphene-based nanostructures with anticipated properties. Pd was co-electrodeposited with Pt at different atomic ratios, and then was anchored with reduced graphene oxide (RGO) simultaneously in the presence of PDDA. The morphologies and structures of the as-prepared PDDA-RGO-PdPt nanocomposites were extensively investigated by transmission electron microscopy (TEM), scanning electron microscopy (SEM), and X-ray diffraction (XRD). The composition was evaluated by energy dispersive X-ray spectrometry (EDS) and inductively coupled plasma–atomic emission spectroscopy (ICP-AES). Raman spectra revealed the surface properties of graphene and its interaction with metallic nanoparticles. Cyclic voltammetric (CV) and chronoamperometric experiments further exhibited their catalytic activity and stability for the electro-oxidation of ethanol in alkaline media, which could be applied as promising electrocatalysts for direct alcohol fuel cells (DAFCs).

1 Introduction

Due to the urgent demands of green energy, biomass-derived alcohols and its clean energy conversion devices, such as direct alcohol fuel cells (DAFCs), have attracted increasing attention, especially in designing and developing efficient anode catalysts. Pt is generally known as one of the best electrocatalysts for fuel cells, however it has some intrinsic drawbacks such as high cost, and vulnerability toward poisoning by intermediate products.[1] Therefore, the efforts on the reduction the amount of Pt have been focused on increasing its intrinsic electrocatalytic activity and durability by alloying it with other metals or seeking alternatives, such as Pt-based,[2] Pd-based[3,4] and other non-noble metal catalysts.[5] Considering the leaching of non-noble metal components,[1] PdPt alloys have been proven to have high electrocatalytic activity, long-term stability and better tolerance.[4] Another effective approach to improve fuel cell performance is to develop novel catalyst supports such as ordered mesoporous carbons (OMCs),[6] carbon nanotubes (CNT)[7] and nitrogen-doped carbon nanotubes (NCNT).[8] Graphene, as a kind of novel single layer carbon material, continues to attract more scientific and technological research interests due to its unique mechanical and electronic properties[9,10] and wide applications,[11,12] especially in electrocatalysis for oxygen reduction[13,14] and alcohol oxidation.[15–17] Therefore, numerous research efforts have been directed towards assembling nanomaterials on graphene sheets. Meanwhile, the immobilization of nanoparticles on graphene sheets is a crucial procedure for constructing the corresponding multifunctional hybrid nanostructure. Graphene-based nanoparticles (NPs) have been prepared by chemical reduction of metals in a graphene aqueous medium,[18] assembly upon strong electrostatic interaction between NPs and functionalized graphene sheets,[19] fabrication of TiO_2-graphene *via* UV-assisted reduction of graphene oxide in TiO_2 suspensions,[20] and so on.

Sonoelectrochemistry, a fast and simple synthetic strategy for the fabrication of nanomaterials,[21–23] has received great success in the preparation of metals,[24–27] alloys,[28] semiconductors[29,30] and conductive polymers.[31] Herein, the hybrid composed of RGO and PdPt alloys was synthesized *via* a sonoelectrochemical route, and the morphology, composition and structure–activity relationship were investigated. The results showed that a PDDA-RGO-Pd_1Pt_3 nanocomposite had excellent electrocatalytic activity and stabilities for the electro-oxidation of ethanol in alkaline media.

2 Experimental

2.1 Materials and reagents

Graphite powder (99.95%, 325 mesh), hexachloroplatinum(IV) acid hydrate ($H_2PtCl_6 \cdot 6H_2O$), palladium(II) chloride ($PdCl_2$), ethanol (C_2H_5OH, anhydrous), potassium nitrate (KNO_3), sodium hydroxide (NaOH) and potassium hydroxide (KOH) were purchased from Chinese Shanghai Regent Co.

[a]Key Laboratory of Analytical Chemistry for Life Science (MOE), School of Chemistry and Chemical Engineering, Nanjing University, Nanjing, 210093, China. E-mail: jjzhu@nju.edu.cn; Fax: +86 25 8359 7204; Tel: +86 25 8359 7204
[b]School of Chemical Engineering, Anhui University of Science and Technology, Huainan, 232001, China

Polydiallyldimethylammonium chloride (PDDA, 20 wt%, in H_2O) and polyvinylpyrrolidone (PVP, Mw = 39000) was purchased from Sigma-Adrich. Hydrazine hydrate, disodium hydrogen phosphate, sodium dihydrogen phosphate, concentrated H_2SO_4, $K_2S_2O_8$, P_2O_5 and H_2O_2 were obtained from Nanjing Chemical Reagents Factory (Nanjing, China). All the chemicals were used as received without further purification. All solutions were prepared with Millipore water.

2.2 Synthesis and characterization

2.2.1 Synthesis of PDDA-RGO. Graphene oxide (GO) was synthesized from natural graphite powder by a modified Hummer's method.[32,33] 0.5 mL of 20 wt% PDDA solution was added into 100 ml of 0.5 mg mL^{-1} GO solution and stirred for 30 min. The freshly-obtained PDDA-GO dispersion was mixed with 0.5 ml 80% hydrazine hydrate and the reduction reaction was performed at 90 °C for 24 h under constant stirring. The resulting PDDA protected reduced graphene oxide (PDDA-RGO) was obtained by filtration and washing with deionized water. For comparison, PVP protected reduced graphene oxide (PVP-RGO) was prepared with the same procedure by adding 3.6 g L^{-1} PVP.

2.2.2 Fabrication of PDDA-RGO-PdPt nanocomposites. A sonoelectrochemical device, which was firstly described by Reissi *et al.*,[34] was employed to prepare PDDA-RGO-PdPt nanocomposites according to ref. 35 with slight modification. Typically, 2 mL of mixture of $PdCl_2$ (56.4 mM) and H_2PtCl_6 (19.3 mM) solution with different volume ratio, 8 mL of KNO_3 (1 M) and 1 mL of PDDA-RGO (0.5 g L^{-1}) were added into 50 mL of PDDA (7.5 g L^{-1}) solution under stirring. The pH value of the mixture was then adjusted to 6.5 with 0.1 M NaOH solution. The PDDA-RGO-PdPt nanocomposites were produced in a sonoelectrochemical reactor. In brief, a titanium horn (ultrasonic liquid processor VC-750, 20 kHz, Sonics & Materials) acts both as a cathode and an ultrasound emitter. This sonoelectrode produces a sonic pulse that is triggered immediately following a current pulse. A CHI 6301B electrochemical workstation (CH Instruments Co., USA) was operated in the pulse current regime (without using a reference electrode). A platinum sheet (1.0 cm × 1.0 cm) was used as a counter electrode. The pulse on time of the current was 0.5 s, the pulse off time of the current was 0.5 s, and the duration of the ultrasonic pulse was 0.3 s, with a current density of 25 mA cm^{-2}, an ultrasound intensity of 20 W approximately, and a reaction time of 4000 s for thorough reaction. The resulting black solution was purified by centrifugation, and the precipitate was washed with Millipore water several times and then dried in air. Hereafter, we will refer to the samples prepared from the $PdCl_2$ (56.4 mM), H_2PtCl_6 (19.3 mM) solution, and the mixtures of them with volume ratios of 3/1, 1/1, and 1/3 as RGO-Pd, RGO-Pt, RGO-Pd_3Pt_1, RGO-Pd_1Pt_1 and RGO-Pd_1Pt_3, respectively.

2.3 Characterization

Characterization was performed *via* X-ray powder diffraction (XRD, Shimadzu XD-3A, with Cu Kα radiation, $\lambda = 0.15418$ nm) and high resolution transmission electron microscopy (HRTEM, JEOL 2100, with a 200 kV accelerating voltage) equipped with an energy dispersive X-ray spectrometer (EDS). The average composition of the PdPt alloy was evaluated using an inductively coupled plasma–atomic emission spectroscopy (ICP-AES, J-A1100). The weight and atomic percentages of the samples were obtained from different volumes ratios of $PdCl_2$ and H_2PtCl_4 solution. Raman spectra of the samples were measured using a Renishaw-in-Via Raman microscope equipped with a ×50 objective using an excitation wavelength of 514.5 nm on 1800-line grating. All samples were deposited on slide glass in powder form without using any solvent.

2.4 Electrochemical experiments

Electrochemical experiments were performed on a CHI 660C electrochemical working station using a standard three-electrode cell. A platinum wire was used as the counter electrode and a saturated calomel electrode (SCE) as the reference. The working electrode was a glassy carbon electrode (GCE, diameter: 3.0 mm) polished with Al_2O_3 powders (Aldrich, 0.05 μm) and rinsed with Millipore water prior to the test. 5 μL of PDDA-RGO or PDDA-RGO-PdPt dispersion, which was prepared by sonicating 10 mg PDDA-RGO-PdPt nanocomposites in 5 mL of Millipore water, and then drop-casting onto a GCE. CV was performed between −0.8 to 0.2 V (*vs.* SCE) in 1.0 M KOH solution with or without 1.0 M ethanol solution at room temperature with a scan rate of 50 mV s^{-1}. Chronoamperometric experiments were carried out at −0.2 V in 1.0 M KOH solution containing 1.0 M ethanol solution at room temperature for 3000 s.

3 Results and discussion

As shown in Fig. 1A, PDDA-RGO with high water-solubility, due to the functional effect of PDDA, has been successfully prepared. More characterization of PDDA-RGO has been shown in our previous report.[33] A series of samples could be facilely obtained *via* sonoelectrochemical method by adding different ratios of the metal precursor solution into reactor. The morphology, structure, particle size were examined by TEM and HRTEM. Fig. 1 shows the TEM images of PDDA-RGO-Pd (B), PDDA-RGO-Pt (C), and PDDA-RGO- Pd_1Pt_3 (D) and their size distributions. The spherical Pd NPs with an average size of 40 nm were composed of small particles of several nanometres (see the insert of Fig. 1B). Pt and Pd_1Pt_3 alloy NPs were uniformly dispersed on the PDDA-RGO sheets with a mean particle size of 2.5 and 4.5 nm, respectively. The typical high-magnification TEM images of PDDA-RGO-Pd_1Pt_3 (Fig. 1E and F) revealed that the d-spacing of adjacent fringes for the alloy NPs was 0.196 nm and 0.226 nm, corresponding to the (2 0 0) and (1 1 1) planes of face-centered-cubic (*fcc*) PdPt alloy,[4] which is smaller than 0.228 nm of pure Pt (1 1 1). It indicated that PdPt alloy NPs could be effectively synthesized, which exhibited uniform shape, excellent size distribution and well dispersion on the unique 2D graphene supports.

The presence of Pd and Pt in the PDDA-RGO-PdPt nanocomposites was also confirmed by EDS analysis as shown in Fig. 2. The intensities of energy peaks assigned to Pd and Pt show a noticeable linear trend with the increase of the Pd/Pt ratio. The peak assigned to Cu in the EDS analysis could be attributed to

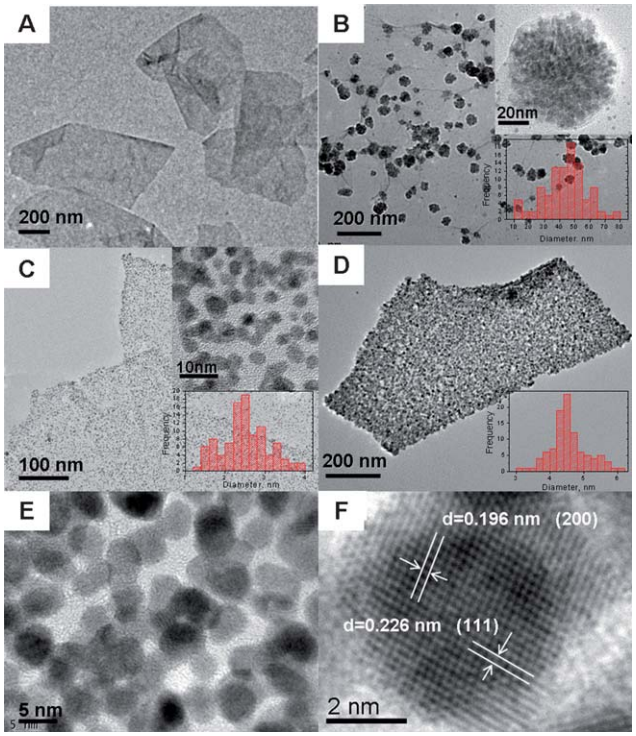

Fig. 1 TEM images of the PDDA-RGO (A), PDDA-RGO-Pd (B), PDDA-RGO-Pt (C), and PDDA-RGO- Pd_1Pt_3 (D) and the HRTEM image of the PDDA-RGO-Pd_1Pt_3 (E, F). Image (F) shows the crystal structure of Pd_1Pt_3 in detail.

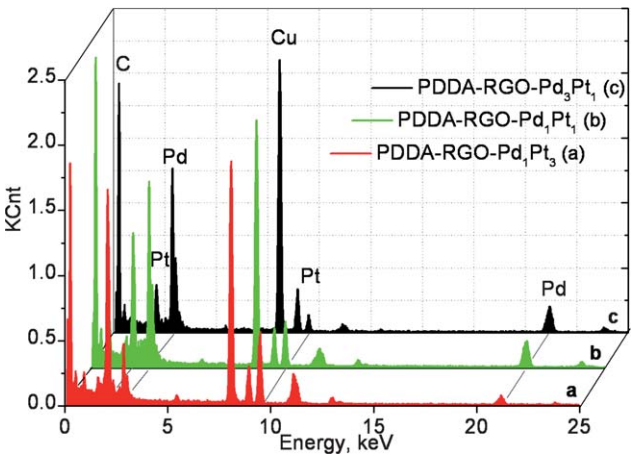

Fig. 2 EDS analysis of the PDDA-RGO-PdPt nanocomposites with different alloy ratios.

the mesh used for the TEM measurement. Furthermore, the composition of PDDA-RGO-PdPt with different alloying ratios was analyzed by ICP-AES. Table 1 shows the average Pt weight content (24.65, 52.89, and 74.06%) and the atomic proportion of Pt (15.3, 37.8 and 69.1%, respectively), which are in good agreement with the results shown in Fig. 2. It indicated that the alloy ratios were roughly consistent with those of the feeding solutions, which presented a facile method to quantitatively control the composition of the alloy and subsequently tune the catalytic activity to obtain an optimum.

Table 1 Composition of PDDA-RGO-PdPt from ICP

Sample	a	b	c
Pt %, weight	74.06	52.89	24.65
Pt %, atom	61.9	37.8	15.3

To further investigate the alloy nature and crystalline structure, the prepared PDDA-RGO-PdPt nanocomposites with different atom proportion were characterized by XRD measurements. As shown in Fig. 3, all the patterns clearly show three main characteristic peaks of face-centered cubic crystalline. The diffraction peaks for Pt, Pt_3Pd_1, Pt_1Pd_1, Pt_1Pd_3 and Pd, were slightly shifted to higher 2θ values with increasing Pd molar ratio, which were 39.83°, 39.96°, 40.04°, 40.10° and 40.18°, respectively, as displayed in the right side of the enlarged (1 1 1) peak. The same trend was also shown in the 2θ of the (2 0 0) and (2 2 0) peaks. Such a consistent shift could be evidence for the alloy formation between Pt and Pd caused by incorporation of Pd atoms to the *fcc* structure of Pt. In addition, the average size of the PdPt alloy NPs is about 4–5 nm calculated by Debye–Scherrer equation, which is consistent with the HRTEM results.

Raman spectroscopy of graphene-based nanocomposites can give important information to distinguish the ordered and disordered carbon structures,[36] number of graphene layers[37] and the interaction between the metal NPs and graphene sheet. As shown in Fig. 4, the Raman spectrum of PDDA-RGO (a) consists of four bands at 1350, 1590, 2690, and 2930 cm^{-1}, which can be designated as D, G, 2D, and 2G bands, respectively. It is found that after hybridization with metal NPs under sonication, the D/G intensity ratio did not change obviously, suggesting that the sonoelectrochemical process did not reduce the size of in-plane sp^2 domains greatly, which determines the electrical conductivity of the graphene sheets. The position of the G-band of RGO-Pt (b), RGO-Pd (c) and RGO-Pd_1Pt_3 (d) has slightly right shifted compared to that of PDDA-RGO (a), which depends on the ionization energy of the metals (with values for Pd and Pt being 5.78 and 6.82 eV), in accordance with a recent

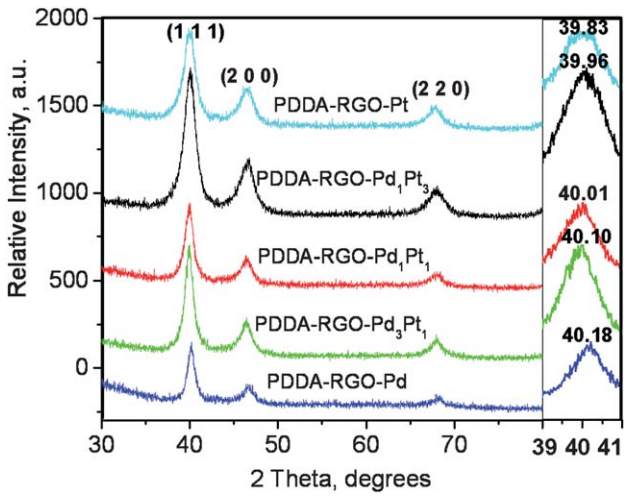

Fig. 3 XRD patterns of PDDA-RGO-PdPt with the atom proportion of Pt is (a) 0%, (b) 15.3%, (c) 37.8%, (d) 61.9% and (e) 100% respectively. The insert shows the magnification of the (1 1 1) peak region.

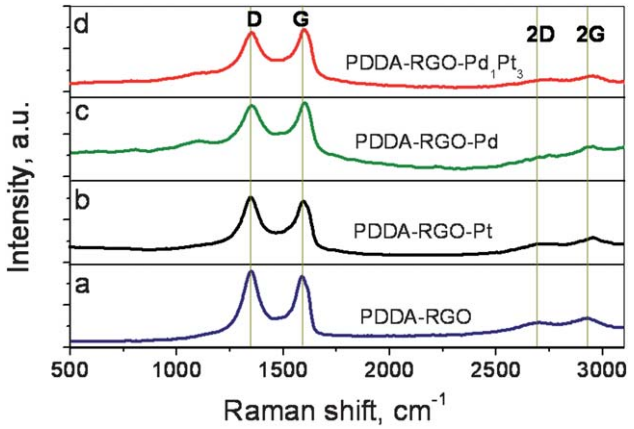

Fig. 4 Raman spectra of (a) PDDA-RGO, (b) PDDA-RGO-Pd, (c) PDDA-RGO-Pt and (d) PDDA-RGO-Pd_1Pt_3.

report.[38] The increase in frequency of the G-bands (2, 7 and 3 cm^{-1}, respectively) revealed the difference in the charge-transfer interactions between the metal NPs and graphene sheet. Furthermore, the shape, position and intensity of 2D-bands can also be taken to reflect the interaction and the dependence on the number of layers. As seen from curves in Fig. 4 (b–d), 2D-bands were centered at 2690 cm^{-1} with a broader expansion compared with that of PDDA-RGO, which indicates the presence of loosely stacked graphene layers intercalated with metal NPs.[36] It can be attributed to the introduction of metal NPs as nano-spacers,[39] which increases the distance between the graphene sheets and prevents the formation of a graphitic structure, thus leading to a high-surface-area and excellent electrical conductivity.

To further confirm the effect of sonication during the formation process of PDDA-RGO-PdPt, a comparison experiment was performed. PdPt NPs were firstly prepared under the same condition by sonoelectrochemistry followed by mixing with PDDA-RGO under thorough stirring. As observed in Fig. 5, it is clear that the simple physical mixing of the as-prepared PdPt NPs with PDDA-RGO sheets resulted in obvious aggregation of the metal NPs and poor dispersion on RGO sheets. On the other hand, the process alternated between the electrodeposition and ultrasonic-assisted assembly with RGO resulted in well distribution of metal NPs. Thus, it further demonstrates that specific interactions between the PdPt NPs and the RGO sheets may be responsible for the dispersion of the NPs, and the sonication played a crucial role in the process.

Thus, a probable evolution of the formation of PDDA-RGO-PdPt under alternate electric and ultrasonic fields, could be demonstrated as follows: firstly, Pd and Pt complex ions diffused towards the surface of the sonoelectrode; then, both of the two ions were co-deposited by a controlled electric pulse and formed PdPt primary particles at the electrode; the primary particles were vibrated off the electrode surface by the pulsed ultrasonic jet streams with the concomitant effects on the dispersion of graphene sheets; simultaneously, the alloy NPs, which dispersed under the ultrasonic field, were directly captured by RGO sheets through ultrasonic assembly[21] coupled with van der Waals[40] and charge-transfer interactions between the PDDA-functionalized RGO and PDDA-capped alloys NPs, as confirmed by Raman spectra. Finally, the PDDA-RGO-PdPt nanocomposites could be obtained by repeating the above procedure. Here, PDDA acts as a stabilizer, disperser and linker in the whole process.

We also tried to synthesize PVP functionalized RGO-PdPt nanocomposites (PVP-RGO-PdPt) under same condition except for adding PVP (3.6 g L^{-1}) instead of PDDA. Unfortunately, the anticipated PdPt alloy NPs were not obtained. As shown in Fig. 6, the particles supported on the RGO sheet could be distinguished as *fcc* Pd NPs with a d-spacing of 0.225 nm corresponding to the (1 1 1) planes. This indicated that Pt perhaps had a lower electro-reduced potential in the presence of PVP resulting in the failure of co-electrodeposition of Pd and Pt.[35]

The influence of the mass ratio of PdPt/RGO on morphology has also been investigated. Considering the catalyst loading, particle size and dispersion on the RGO, the typical synthesis of PDDA-RGO-PdPt was performed at a ratio of 8.65 mg mg^{-1}. The average loading of Pd_1Pt_3 catalyst supported on RGO was calculated from the stoichiometric ratio of metal precursors, namely 17.3, 8.65, 1.73 mg mg^{-1} (PdPt/RGO), respectively. As seen in Fig. 7, the metal loading increases with ratio of PdPt/RGO in the solution, resulting in partial agglomeration. The size of the PdPt alloy NPs decreases, because the deposition potential decreases with increasing concentration of Pd and Pt complex, resulting in an increased nucleation rate.

Hydrogen adsorption–desorption peaks of the cyclic voltammograms are usually used to evaluate electrochemically active surface area (ECSA) of the catalyst. The ECSA of the PDDA-Pd_1Pt_3 and PDDA-RGO- Pd_1Pt_3 nanocomposite modified electrodes could be estimated using the formula ECSA $=Q_H/Q_{0,H}$ from the average charge transfer (Q_H) based on integrated values

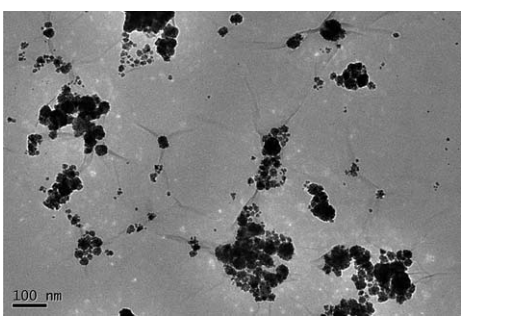

Fig. 5 PDDA-RGO-Pd_3Pt_1 prepared *via* two steps: sonoelectrosynthesis of Pd_3Pt_1 NPs followed by mixing with PDDA-RGO under thorough stirring.

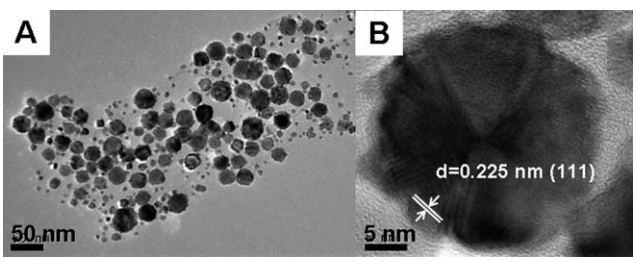

Fig. 6 TEM images of the PVP-RGO-PdPt (A) and HRTEM image of the crystal structure in detail (B).

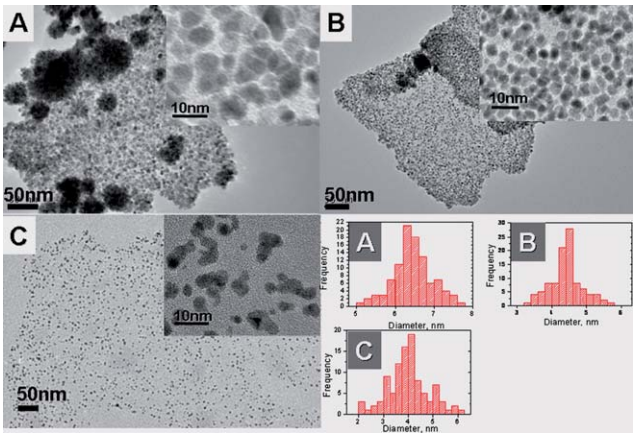

Fig. 7 TEM images and corresponding size distribution patterns of the PDDA-RGO-Pd_1Pt_3 nanocomposites synthesized with different ratios of metal/RGO: (A) 17.3 mg mg^{-1}, (B) 8.65 mg mg^{-1}, (C) 1.73 mg mg^{-1}. Insets are magnified TEM figures.

of hydrogen adsorption–desorption in the range −0.7∼−1.1 V.[41] Assuming the charge per real area of catalyst with monolayer adsorption of hydrogen is $Q_{0,H} = 210\ \mu C\ cm^{-2}$, then according to the CV curves in Fig. 8, the estimated electrochemically active special surface area (ECSSA) values are 19.38 $cm^2\ cm^{-2}$ (PDDA-Pd_1Pt_3 modified electrode), 27.81 $cm^2\ cm^{-2}$ (PDDA-RGO-Pd_1Pt_3 modified electrode), respectively (see Table 2). This suggests that the PDDA-RGO-Pd_1Pt_3 modified electrode had the higher ECSSA value, which is consistent with the improved adhesion, accessibility and dispersion of the catalytically active sites in the nanocomposites, which also is expected to show better performance in electrocatalysis. It is due to the fact that PdPt NPs are smaller and more uniformly dispersed onto the surface of RGO sheets, which is consistent with the results in TEM analysis (see Fig. 1D and E).

The electrocatalytic activity of ethanol oxidation on RGO-supported Pt and PdPt alloy NPs was characterized by cyclic voltammetry (see Fig. 9A and B) and linear sweep voltammetry (Fig. 9C) in 0.1 M KOH solution containing 1.0 M ethanol at a scan rate of 50 mV s^{-1}, and the corresponding data were summarized in Table 3. The voltammograms of each sample became similar and stable after the twentieth cycle. The efficiency

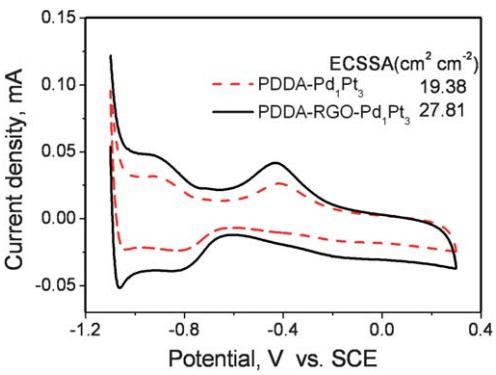

Fig. 8 Cyclic voltammograms in 1 M KOH at PDDA-Pd_1Pt_3 (dash line) and PDDA-RGO-Pd_1Pt_3 (straight line) modified GCE with the same amount of metal loading.

Table 2 The calculated results of ECSA and ECSSA from CV in Fig. 8

Electrode	Loading, mg cm^{-2}	Q_H, mC cm^{-2}	ECSA, $cm^2\ mg^{-1}$	ECSSA, cm cm^{-2}
PDDA-Pd_1Pt_3	0.476	4.07	40.72	19.38
PDDA-RGO-Pd_1Pt_3	0.488	5.84	56.99	27.81

of the PDDA-RGO-PdPt nanocomposites on ethanol oxidation and tolerance to the poisoning species was compared by using the ratio of the forward peak current density to the backward reverse peak current (I_f/I_b). As shown in Fig. 9A, the current increases slowly at the beginning of the forward scan, and then quickly rises up when the potential is higher than −0.5 V, while oxidation occurred at approximately −0.1 V. The current density is directly proportional to the amount of oxidized ethanol. The current density of PDDA-RGO-PdPt is approximately 6.7 mA cm^{-2}, nearly 1.5 times more than that of the PdPt alloy without RGO. In the reverse potential sweep, an oxidation peak at around −0.19 V was observed, putatively associated with the removal of the partially oxidized intermediates, such as acetaldehyde and acetic acid, and formed on the electrode in the forward sweep.[42] As shown in Fig. 9A, the I_f/I_b ratio of PDDA-RGO-PdPt is 1.26, which is higher than that of the PdPt NPs (0.89), indicating that the graphene effectively enhances the complete oxidation of ethanol to CO_2, and fewer CO-like carbonaceous species accumulate on the electrode surface.[43] This result suggests that graphene plays a critical role in promoting the ethanol oxidation of PdPt NPs, and could be attributed to the intrinsic electron transfer characteristic of RGO and good dispersion of PdPt NPs on the RGO sheets.

It is well known that the incorporation of Pt with other metals could improve its catalytic activity to alcohols and the tolerance to intermediate carbonaceous species.[44] The compositional effects of the PdPt alloy on the catalytic activity and stability for the oxidation of ethanol have been further illustrated by CV and LSV in Fig. 9 B and C. The ethanol oxidation current density (I_f) on PDDA-RGO-PdPt was higher than that on PDDA-RGO-Pd or PDDA-RGO-Pt, and the I_f depending on the alloy composition first increases, and then decreases as the Pd content changes from 0 to 100% (see Fig. 9B); and the PDDA-RGO-Pd_1Pt_3 with a Pt atomic proportion of 0.619 exhibited much higher activity and better stability. This is in good agreement with previous studies on Pt-based alloys.[45] Furthermore, as indicated by dashed lines in Fig. 9C, the corresponding potential on PDDA-RGO-Pd_1Pt_3 is much lower than the others at a given oxidation current density. It means that PDDA-RGO-Pd_1Pt_3 exhibits better performance for ethanol electro-oxidation at all applied potentials (from −0.6 to −0.2 V). Such a large enhanced catalytic activity for ethanol can be attributed to the bifunctional mechanism of the alloy catalyst.[46] The role of Pd is as a catalytically enhancing agent, which can modify the electronic properties of the Pt.[47] However, the activity of the alloy greatly decreases when more Pd is added into the alloy. This may be a result of over-dilution of the active sites of Pt.[48]

The stability of ethanol oxidation on PDDA-Pd_1Pt_3, PDDA-RGO-Pt, PDDA-RGO-Pd and PDDA-RGO-Pd_1Pt_3 modified electrodes was further investigated by chronoamperometry at a potential of −0.2 V in 0.1 M KOH in the presence of 1 M

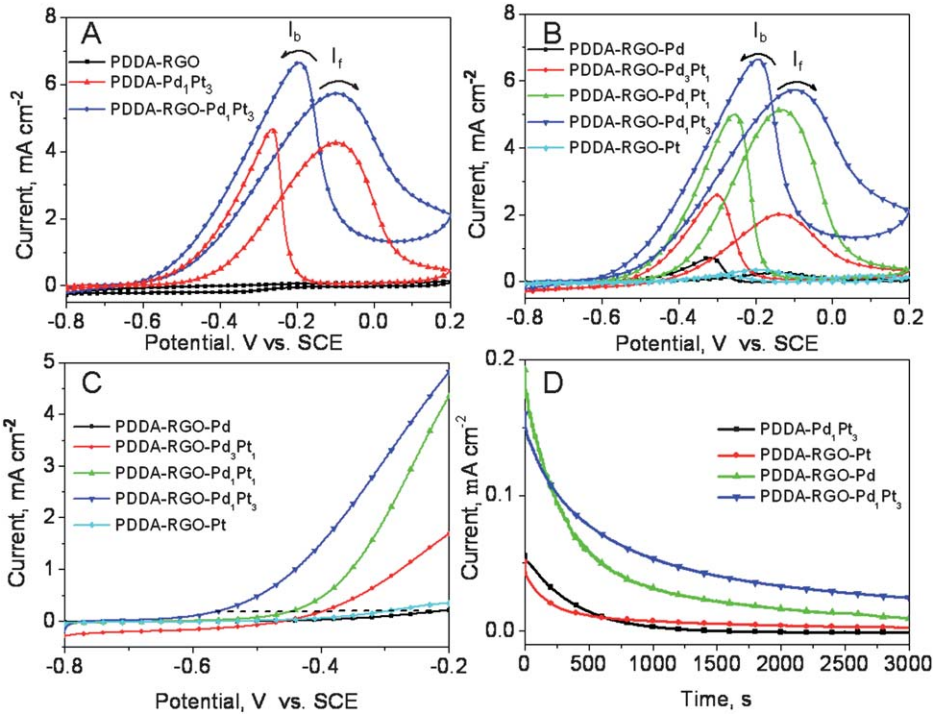

Fig. 9 (A) CVs of the PDDA-RGO, PDDA-Pd_1Pt_3 and PDDA-RGO-Pd_1Pt_3 alloy; (B) CVs, (C) linear sweep voltammetry and (D) chronoamperometry of the PDDA-RGO-PdPt with different alloy ratios modified electrode in 0.1 M KOH solution containing 1.0 M ethanol at 50 mV s^{-1}.

ethanol. As shown in Fig. 9.D, the polarization current shows a rapid decline, which can be explained in terms of a poisoning mechanism of the intermediate species during the ethanol electrooxidation.[49] However, the current decay on both PDDA-Pd_1Pt_3, PDDA-RGO-Pd and PDDA-RGO-Pd_1Pt_3 modified electrodes is slower than that on the RGO-Pt modified electrode. At the end, the oxidation current on the PDDA-RGO-Pd_1Pt_3 modified electrode is considerably higher than the others, suggesting that the alloying of PdPt NPs and the formation of metal–graphene nanocomposites enhance both the electrocatalytic activity and stability of the catalyst.

4 Conclusion

In summary, we have illuminated a facile strategy to fabricate graphene-supported PdPt nanoparticles *via* sonoelectrochemical technique, where the sonication played a crucial role in the dispersion of graphene sheets, regenerating the electrode by vibrating off the electrodeposited alloy NPs and direct assembling the NPs onto RGO. The as-prepared PDDA-RGO-Pd_1Pt_3 nanocomposites combined the unique properties of 2D graphene with alloying effects, and have exhibited significantly enhanced catalytic activity and stability towards ethanol electrooxidation, demonstrating its potential application as effective electro-catalysts for DAFCs in alkaline conditions. Considering the well-established sonoelectrochemical method in the preparation of nanomaterials, the present strategy may be applied in developing other various graphene based functional nanocomposites as well.

Acknowledgements

We are grateful to the financial support of National Natural Science Foundation of China (No. 50972058,20821063),"973" Program (No. 2011CB933502), the International S&T Cooperation Projects of China (2010DFA42060) and JJS also thanks the support of Natural Science Foundation of Anhui Educational Committee (KJ2008B188).

Table 3 Comparison of electrocatalytic activity of PDDA-RGO-PdPt alloy with different atomic ratios

	Forward sweep		Backward sweep		
Samples	I_f, mA cm^{-2}	E, V	I_b, mA cm^{-2}	E, V	I_f/I_b ratio
PDDA-Pd_1Pt_3	4.2	−0.10	4.7	−0.21	0.89
PDDA-RGO-Pd	0.2	−0.16	0.8	−0.32	0.25
PDDA-RGO-Pd_3Pt_1	2.0	−0.14	2.6	−0.30	0.77
PDDA-RGO-Pd_1Pt_1	5.1	−0.13	4.9	−0.27	1.04
PDDA-RGO-Pd_1Pt_3	6.7	−0.10	5.3	−0.19	1.26
PDDA-RGO-Pt	0.3	−0.18	0.2	−0.25	1.50

References

1 E. Antolini, T. Lopes and E. R. Gonzalez, *J. Alloys Compd.*, 2008, **461**, 253–262.
2 A. C. Chen and P. H. Hindle, *Chem. Rev.*, 2010, **110**, 3767–804.
3 E. Antolini, *Energy Environ. Sci.*, 2009, **2**, 915–931.
4 C. Bianchini and P. K. Shen, *Chem. Rev.*, 2009, **109**, 4183–4206.
5 A. Serov and C. Kwak, *Appl. Catal., B*, 2009, **90**, 313–320.
6 H. Chang, S. H. Joo and C. Park, *J. Mater. Chem.*, 2007, **17**, 3078–88.
7 I. Dumitrescu, P. R. Unwin and J. V. Macpherson, *Chem. Commun.*, 2009, 6886–6901.
8 K. P. Gong, F. Du, Z. H. Xia, M. Durstock and L. M. Dai, *Science*, 2009, **323**, 760–764.
9 D. Li and R. B. Kaner, *Science*, 2008, **320**, 1170.
10 R. M. Westervelt, *Science*, 2008, **320**, 324.
11 X. M. Geng, L. Niu, Z. Y. Xing, R. S. Song, G. T. Liu, M. T. Sun, G. S. Cheng, H. J. Zhong, Z. H. Liu, Z. J. Zhang, L. F. Sun, H. X. Xu, L. Lu and L. W. Liu, *Adv. Mater.*, 2010, **22**, 638–642.
12 W. R. Yang, K. R. Ratinac, S. P. Ringer, P. Thordarson, J. J. Gooding and F. Braet, *Angew. Chem., Int. Ed.*, 2010, **49**, 2114–2138.
13 F. H. Li, H. F. Yang, C. S. Shan, Q. X. Zhang, D. X. Han, I. Ivaska and L. Niu, *J. Mater. Chem.*, 2009, **19**, 4022–4025.
14 Y. Y. Shao, S. Zhang, C. M. Wang, Z. M. Nie, J. Liu, Y. Wang and Y. H. Lin, *J. Power Sources*, 2010, **195**, 4600–4605.
15 Y. M. Li, L. H. Tang and J. H. Li, *Electrochem. Commun.*, 2009, **11**, 846–849.
16 B. Seger and P. V. Kamat, *Fuel Cells*, 2009, **113**, 7990–7995.
17 Y. J. Li, W. Gao, L. J. Ci, C. M. Wang and P. M. Ajayan, *Carbon*, 2010, **48**, 1124–1130.
18 R. Muszynski, B. Seger and P. Kamat, *J. Phys. Chem. C*, 2008, **112**, 5263–5266.
19 W. J. Hong, H. Bai, Y. X. Xu, Z. Y. Yao, Z. Z. Gu and G. Q. Shi, *J. Phys. Chem. C*, 2010, **114**, 1822–1826.
20 G. Williams, B. Seger and P. V. Kamat, *ACS Nano*, 2008, **7**, 1487–1491.
21 A. Gedanken, *Ultrason. Sonochem.*, 2004, **11**, 47–55.
22 V. Sáez and T. J. Mason, *Molecules*, 2009, **14**, 4284–4299.
23 J. H. Bang and K. S. Suslick, *Adv. Mater.*, 2010, **22**, 1039–1059.
24 J. J. Zhu, S. Liu, O. Palchik, Y. Koltypin and A. Gedanken, *Langmuir*, 2000, **16**, 6396–6399.
25 I. Haas, S. Shanmugam and A. Gedanken, *Chem.–Eur.J.*, 2008, **14**, 4696–4703.
26 Q. M. Shen, L. P. Jiang, H. Zhang, Q. H. Min, W. H. Hou and J. J. Zhu, *J. Phys. Chem. C*, 2008, **112**, 16385–16392.
27 C. Mahendiran, R. Ganesan and A. Gedanken, *Eur. J. Inorg. Chem.*, 2009, 2050–2053.
28 M. Dabala, B. G. Pollet, V. Zin, E. Campadello and T. J. Mason, *J. Appl. Electrochem.*, 2008, **38**, 395–402.
29 X. F. Qiu, C. Burda, R. L. Fu, L. Pu, H. Y. Chen and J. J. Zhu, *J. Am. Chem. Soc.*, 2004, **126**, 16276–16277.
30 Q. M. Shen, L. P. Jiang, J. J. Miao, W. H. Hou and J. J. Zhu, *Chem. Commun.*, 2008, 1683–1685.
31 M. Atobe, K. Ishikawa, R. Asami and T. Fuchigami, *Angew. Chem., Int. Ed.*, 2009, **48**, 6069–6072.
32 W. S. Hummers and R. E. Offeman, *J. Am. Chem. Soc.*, 1958, **6**, 1339.
33 K. P. Liu, J. J. Zhang, G. H. Yang, C. M. Wang and J. J. Zhu, *Electrochem. Commun.*, 2010, **12**, 402–405.
34 J. Reisse, H. Francois, J. Vandercammen, O. Fabre, A. Kirsch-de Mesmaeker, C. Maerschalk and J. L. Delplancke, *Electrochim. Acta*, 1994, **39**, 37–39.
35 Q. M. Shen, Q. H. Min, J. J. Shi, L. P. Jiang, J. R. Zhang, W. H. Hou and J. J. Zhu, *J. Phys. Chem. C*, 2009, **113**, 1267–1273.
36 M. S. Dresselhaus, A. Jorio, M. Hofmann, G. Dresselhaus and R. Saito, *Nano Lett.*, 2010, **10**, 751–758.
37 D. Graf, F. Molitor, K. Ensslin, C. Stampfer, A. Jungen, C. Hierold and L. Wirtz, *Nano Lett.*, 2007, **7**, 238–242.
38 K. S. Subrahmanyam, A. K. Manna, S. K. Pati and C. N. R. Rao, *Chem. Phys. Lett.*, 2010, **497**, 70–75.
39 Y. C. Si and E. T. Samulski, *Chem. Mater.*, 2008, **20**, 6792–6797.
40 V. Georgakilas, D. Gournisb, V. Tzitziosa, L. Pasquato, D. M. Guldie and M. Prato, *J. Mater. Chem.*, 2007, **17**, 2679.
41 X. Y. Zhang, W. Lu, J. Y. Da, H. T. Wang, D. Y. Zhao and P. A. Webley, *Chem. Commun.*, 2009, 195–197.
42 H. F. Wang and Z. P. Liu, *J. Phys. Chem. C*, 2007, **111**, 2157–12160.
43 S. J. Guo, S. J. Dong and E. K. Wang, *ACS Nano*, 2010, **4**, 547–555.
44 Y. H. Bing, H. S. Liu, L. Zhang, D. Ghosh and J. J. Zhang, *Chem. Soc. Rev.*, 2010, **39**, 2184–2202.
45 W. M. Wang, Q. H. Huang, J. Y. Liu, Z. Q. Zou, Z. L. Li and H. Yang, *Electrochem. Commun.*, 2008, **10**, 1396–1399.
46 Q. Yuan, Z. Y. Zhou, J. Zhuang and X. Wang, *Chem. Commun.*, 2010, **46**, 1491–1493.
47 V. Stamenkovic, T. J. Schmidt, P. N. Ross and N. M. Markovic, *J. Phys. Chem. B*, 2002, **106**, 11970–11979.
48 S. H. Chang, W. N. Su, M. H. Yeh, C. J. Pan, K. L. Yu, D. G. Liu, J. F. Lee and B. J. HWang, *Chem.–Eur. J.*, 2010, **16**, 11064–11071.
49 A. V. Tripovic', K. D. Popovic' and J. D. Lovic', *Electrochim. Acta*, 2001, **46**, 3163–3173.